

# Effect of Zn substitution on structural, dielectric and magnetic properties of nanocrystalline $\text{Co}_{1-x}\text{Zn}_x\text{Fe}_2\text{O}_4$ for potential high density recording media

K. Praveena<sup>1</sup> · K. Sadhana<sup>2</sup> · Hsiang-Lin Liu<sup>1</sup> · S. R. Murthy<sup>3</sup>

Received: 11 May 2016 / Accepted: 19 July 2016 / Published online: 25 July 2016  
© Springer Science+Business Media New York 2016

**Abstract**  $\text{Co}_{1-x}\text{Zn}_x\text{Fe}_2\text{O}_4$  ( $0 \leq x \leq 1$ ) nanopowders were synthesized using microwave hydrothermal method. The synthesized powders were characterized by X-ray diffraction and transmission electron microscope (TEM). The average particle size was obtained from TEM and it is found to be 17 nm. Then powders were sintered using microwave sintering method at 900 °C/15 min. The real part of permittivity varies as Zn concentration increases and the resonance frequency was observed at much higher frequencies ( $>1$  GHz) and there is a significant decrease in the loss factor. The dielectric parameters were observed to decrease with the increased Zn contents. The frequency dependent dielectric properties of all these nanomaterials have been explained qualitatively in accordance with Koop's phenomenological theory. The magnetic permeability spectra exhibit resonance and anti-resonance type behaviour. Lower reduced remnant magnetization ( $M_r/M_s$ ) values ( $x < 0.5$ ) suggest that all the samples have uniaxial anisotropy. The increasing trend of magnetic parameters (coercivity and retentivity) is consistent with crystallinity. The moderate magnetization and high coercivity are enough to attain considerable signal to noise ratio in high density recording media.

## 1 Introduction

Since last two decades, the nanomaterials have been extensively studied worldwide because of their unique properties that are not exhibited by the corresponding bulk materials. Among various nanomaterials, the spinel ferrite ( $\text{MFe}_2\text{O}_4$ ,  $\text{M} = \text{Ni}, \text{Co}, \text{Mn}, \text{Zn}, \text{etc.}$ ) nanocrystals have become immensely popular magnetic materials due to some unique properties exhibited by these materials. These properties include large magnetocrystalline anisotropy, high coercivity, mechanical harness and chemical stability [1–3]. These specific properties make them useful in various technical applications such as magnetic recording devices, magnetic storage devices, magnetic resonance imaging enhancement, catalysis, drug targeting and gas sensors [4–7]. Furthermore, nanoferrites are gaining substantial interest among the research community as they exhibit a relationship between magnetic properties and their crystal structure. It is reported in literature that small crystalline size significantly improved the electrical and magnetic properties of ferrites [8].

Recent studies have shown that reduction in the size of magnetic materials may lead to novel properties improved better than to the properties of the bulk materials, due to small volume (superparamagnetism) [9] or high surface/volume ratio (spin canting) [10].

The synthesis of nanocrystalline ferrites have been extensively investigated in recent years because of their potential applications in high density magnetic recording, and magnetic fluids [11] etc. Various preparation techniques such as sol–gel [12], micro emulsion method [13], hydrothermal techniques [14], co-precipitation [2], solution combustion [15], mechanical alloying [16] and microwave-hydrothermal method etc., [17] are being used to synthesize nanoparticles.

✉ K. Praveena  
praveenaou@gmail.com

<sup>1</sup> Department of Physics, National Taiwan Normal University, Taipei 11677, Taiwan

<sup>2</sup> Department of Physics, University College of Science, Osmania University, Saifabad, Hyderabad 500 004, India

<sup>3</sup> Department of Physics, University College of Science, Osmania University, Hyderabad 500 007, India

Although the hydrothermal method is very versatile, one of the main drawbacks is, the hydrothermal method requires prolonged reaction time at a low temperature (below 200 °C) to obtain the ferrite powders. For this reason, the introduction of microwave heating to the conventional-hydrothermal (C-H) method is advantageous for the synthesis of various ceramic powders, and this was named as Microwave-Hydrothermal (M-H) by Komarneni et al. [17]. The main advantages of this process over conventional-hydrothermal process are (a) the rapid heating to treatment temperature saves time and energy, (b) the kinetics of the reaction are enhanced by one to two orders of magnitude, (c) lead to the formation of novel phases, and (d) lead to selective crystallization.

According to recent research on  $\text{Zn}^{2+}$  substituted  $\text{CoFe}_2\text{O}_4$  nanoferrite ( $\text{Co}_{1-x}\text{Zn}_x\text{Fe}_2\text{O}_4$ ) exhibited improved magnetic and electrical properties [18]. Substitution of  $\text{Co}^{2+}$  with  $\text{Zn}^{2+}$  leads to introduction of nonmagnetic  $\text{Zn}^{2+}$  ions into A sites, thus increasing saturation magnetization,  $M_s$  leading to an increased magnetization [19]. In this paper, we have synthesized  $\text{Co}_{1-x}\text{Zn}_x\text{Fe}_2\text{O}_4$  ( $x = 0, 0.2, 0.4, 0.6, 0.8$  and 1) using M-H method. The obtained nanoparticles have many potential application as a head in recording media, since these materials fulfil the major requirements: materials should magnetically soft, high permeability, low coercivity and high magnetization. The coercivity of all the substituted samples was found to be a few hundred oersteds which is one of the necessary conditions for recording media. The effect of zinc on dielectric and magnetic properties of  $\text{CoFe}_2\text{O}_4$  will be discussed in this paper.

## 2 Experimental

Nanopowders of stoichiometric composition  $\text{Co}_{1-x}\text{Zn}_x\text{Fe}_2\text{O}_4$  ( $0 \leq x \leq 1$ ) were prepared using microwave hydrothermal method. High purity (sigma, 99.99 %) of cobalt nitrate [ $\text{Co}(\text{NO}_3)_2 \cdot 6\text{H}_2\text{O}$ ], zinc nitrate [ $\text{Zn}(\text{NO}_3)_2 \cdot 6\text{H}_2\text{O}$ ] and iron nitrate [ $\text{Fe}(\text{NO}_3)_3 \cdot 9\text{H}_2\text{O}$ ] were dissolved in de-ionized water. An aqueous NaOH was added dropwise to the solution until pH ( $\sim 13$ ) was obtained. The mixture was then transferred into Teflon lined vessel and kept in microwave digestion system (Model MDS-2000, CEM Corp., Mathews, NC). This system uses 2.45 GHz microwaves and can operate at 0–100 % full power ( $1200 \pm 50$  W). The system is controlled by pressure and can attain maximum pressure of 200 psi, which is equivalent to 194 °C. In the present investigation all the samples were synthesized at 140 °C/15 min. The time, pressure and powder were computer controlled. The products obtained were filtered and then washed repeatedly with de-ionized water, followed by freeze drying overnight. The prepared

powders were weighed and the percentage yields were calculated from the expected and the amount that was actually crystallized. The particle sizes of as-synthesized powders were estimated by Transmission Electron Microscope (TEM, JEOL). FTIR transmission spectra were recorded on Bruker Tensor 27 model Infrared Spectrophotometer from 4000 to 400  $\text{cm}^{-1}$ . The sintered samples were characterized by Phillips PANalytical X'pert powder X-ray diffraction (XRD) with Cu-K $\alpha$  ( $\lambda = 1.5406$  Å) radiation. The powders were pressed at 2.5  $\text{kg}/\text{cm}^2$  into pellets by adding 2 wt% of polyvinyl alcohol (PVA) which acts as a binder (8 mm diameter and 1.5 mm thickness). The green compacts were sintered using microwave furnace at 900 °C/15 min in air, binder will burnt out at 300 °C. Sintering is defined as a thermal treatment for bonding particles into a coherent, predominantly solid structure via mass transport events on the atomic scale [20].

The lattice constant ( $a$ ) for the cubic crystal system was calculated using the equation  $a = d\sqrt{h^2 + k^2 + l^2}$  where ( $h$   $k$   $l$ ) are the Miller indices of the diffraction peak and ' $d$ ' is the interplanar spacing. The average crystallite size was calculated from Scherer formula  $D_m = K\lambda/\beta \cos \theta$  where  $K$  is a constant,  $\lambda$  radiation wavelength  $\beta$  is full width half maxima (FWHM) and  $\theta$  is the diffraction angle. The theoretical density ( $d_{\text{X-ray}}$ ) of these ferrites were calculated from the values of lattice parameters by using the relation  $d_{\text{X-ray}} = \frac{8M}{Na^3}$   $\text{g}/\text{cm}^3$  where 8 is the number of formula units in a unit cell,  $M$  is the molecular weight and  $N$  is the Avogadro number and ' $a$ ' is lattice constant. The distance between magnetic ions, hopping lengths in octahedral sites and tetrahedral sites is given by the following relation [21]  $L_A = a\frac{\sqrt{3}}{4}$ ;  $L_B = a\frac{\sqrt{2}}{4}$ . The morphology of the powders was studied using field emission scanning electron microscopy (FE-SEM, ZEISS). The room temperature complex permittivity ( $\epsilon'$  and  $\epsilon''$ ) and permeability ( $\mu'$  and  $\mu''$ ) were measured over a wide frequency range from 1 MHz to 1.8 GHz using Agilent RF impedance analyser 4291B. Room temperature magnetic measurements were obtained from a super conducting quantum interference device (SQUID).

## 3 Results and discussion

### 3.1 Structural and morphological studies

Figure 1a shows TEM image of  $\text{Co}_{0.4}\text{Zn}_{0.6}\text{Fe}_2\text{O}_4$ , and the particle size is  $\sim 17$  nm. The ferrites exhibited more or less spherical morphology with uniform size. All the samples were synthesized of pH of  $\sim 13$ , were obtained with 95 %

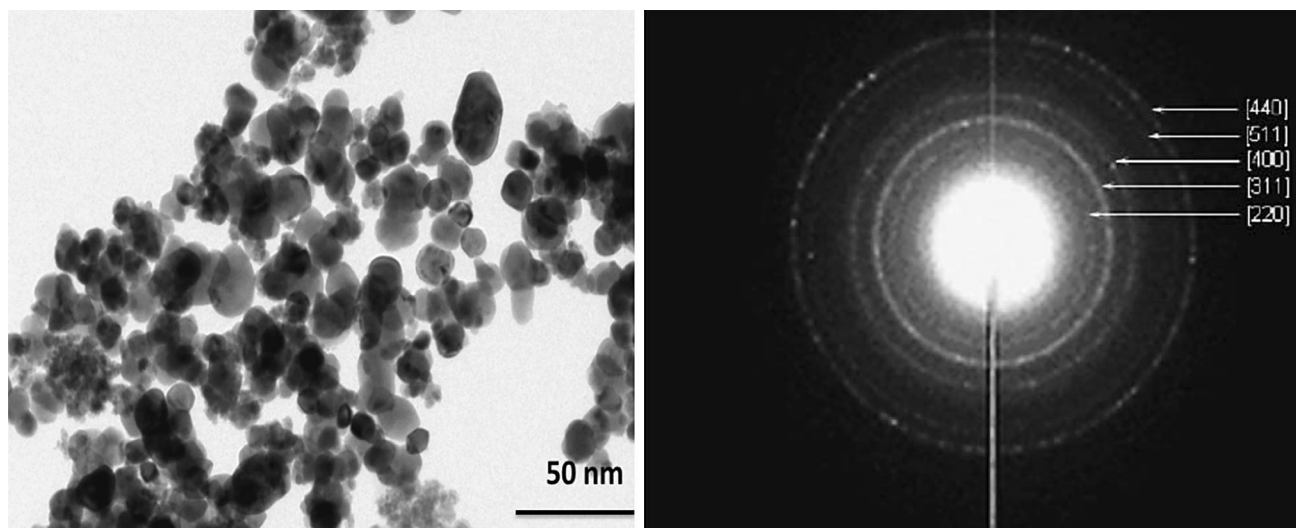


**Fig. 1** **a** Bright field TEM image of the  $\text{Co}_{0.4}\text{Zn}_{0.6}\text{Fe}_2\text{O}_4$ . **b** SAED pattern of  $\text{Co}_{0.4}\text{Zn}_{0.6}\text{Fe}_2\text{O}_4$

yield. The Selected Area Electron Diffraction (SAED) ring pattern (Fig. 1b) of the nanoparticles of  $\text{Co}_{0.4}\text{Zn}_{0.6}\text{Fe}_2\text{O}_4$  is well resolved at (220), (311), (400), (422), (511), (440) reflections of XRD patterns.

Figure 2a shows the XRD pattern for the sintered samples at  $900\text{ }^\circ\text{C}/15\text{ min}$ . It is clear that samples possess single spinel nature. The XRD patterns show (220), (311), (400), (422), (333) and (440) planes which belong to cubic spinel structure. The XRD peaks are sharp and intense, XRD patterns that peak position slightly shifts towards lower angle, indicating the change in the inter-planar spacing ( $d$ ) values. The lattice constant was calculated using inter-planar spacing ( $d$ ) values and Miller indices ( $hkl$ ) values, with an accuracy of  $\pm 0.002\text{ \AA}$ . The values of lattice constant vary from 8.388 to 8.44  $\text{\AA}$  and are given in Table 1. It is observed that lattice constant ' $a$ ' increases linearly with zinc content ( $x$ ). The variation of lattice constant of the present system can be explained on the basis of difference in ionic radii of the substituted ions. The ionic radii of  $\text{Zn}^{2+}$  (0.82  $\text{\AA}$ ) [22] are larger than that of  $\text{Co}^{2+}$  (0.78  $\text{\AA}$ ) ions. The increase in lattice constant with zinc substitution obeys the Vegard's law [23]. The uniform increase in lattice constant with zinc substitution indicates that lattice expands without disturbing the symmetry of lattice. To calculate the average crystallite size from the broadening of the XRD peaks of  $\text{Co}_{0.4}\text{Zn}_{0.6}\text{Fe}_2\text{O}_4$ , the Rietveld refinement was applied. The quality of the refinement is quantified by the corresponding Figure of merit: profile residual ( $R_p$ ), weighted profile residual ( $R_{wp}$ ) and goodness of fit ( $\chi^2$ ) [24]. Figure 2b shows the Rietveld refinement of microwave sintered  $\text{Co}_{0.4}\text{Zn}_{0.6}\text{Fe}_2\text{O}_4$ . Its lattice constant is 8.4  $\text{\AA}$ .

The bulk density of the specimens has been determined by the Archimedes method. The values of the bulk densities are given in Table 1. The bulk density was found to increase with Zn content ( $x$ ). In the present series the molecular weight of Co–Zn spinel ferrite increases with zinc substitution and volume of the unit cell also increases, but the rate of increase of molecular weight is more than that of volume. Therefore, the bulk density increases with zinc substitution in the present case. The values of X-ray density ' $d_x$ ' are given in Table 1. It has been observed that X-ray density increases with increasing zinc content ( $x$ ), which is related to the lattice constant. In the present series of Co–Zn spinel ferrites, the lattice constant increases with  $\text{Zn}^{2+}$  composition ( $x$ ). Due to increase in lattice constant, X-ray density should have been decreased, but in the present case molecular weight increases which overtake the increase in volume of the unit cell and hence X-ray density increases with Zn content ( $x$ ). The percentage porosity ' $P$ ' of the sample was calculated using the values of X-ray density and bulk density. Table 1 gives the values of porosity. The density of the samples increases with increase in Zn composition ( $x$ ). The increase of the density is correlated with the atomic weight of the  $\text{Zn}^{2+}$  ions instead of  $\text{Co}^{2+}$  ions of lower density. The atomic weight of Zn and Co ions is 65.39 and 58.933 amu respectively. This is the evidence of accelerated densification during the sintering process which led to reduction of porosity [25]. The low values of porosity indicate the highly dense structure of the prepared samples of Co–Zn spinel ferrite.

The distance between magnetic ions at tetrahedral A ( $L_A$ ) and octahedral B ( $L_B$ ) sites was calculated using the relations of ref [26]. The variation of hopping length  $L_A$

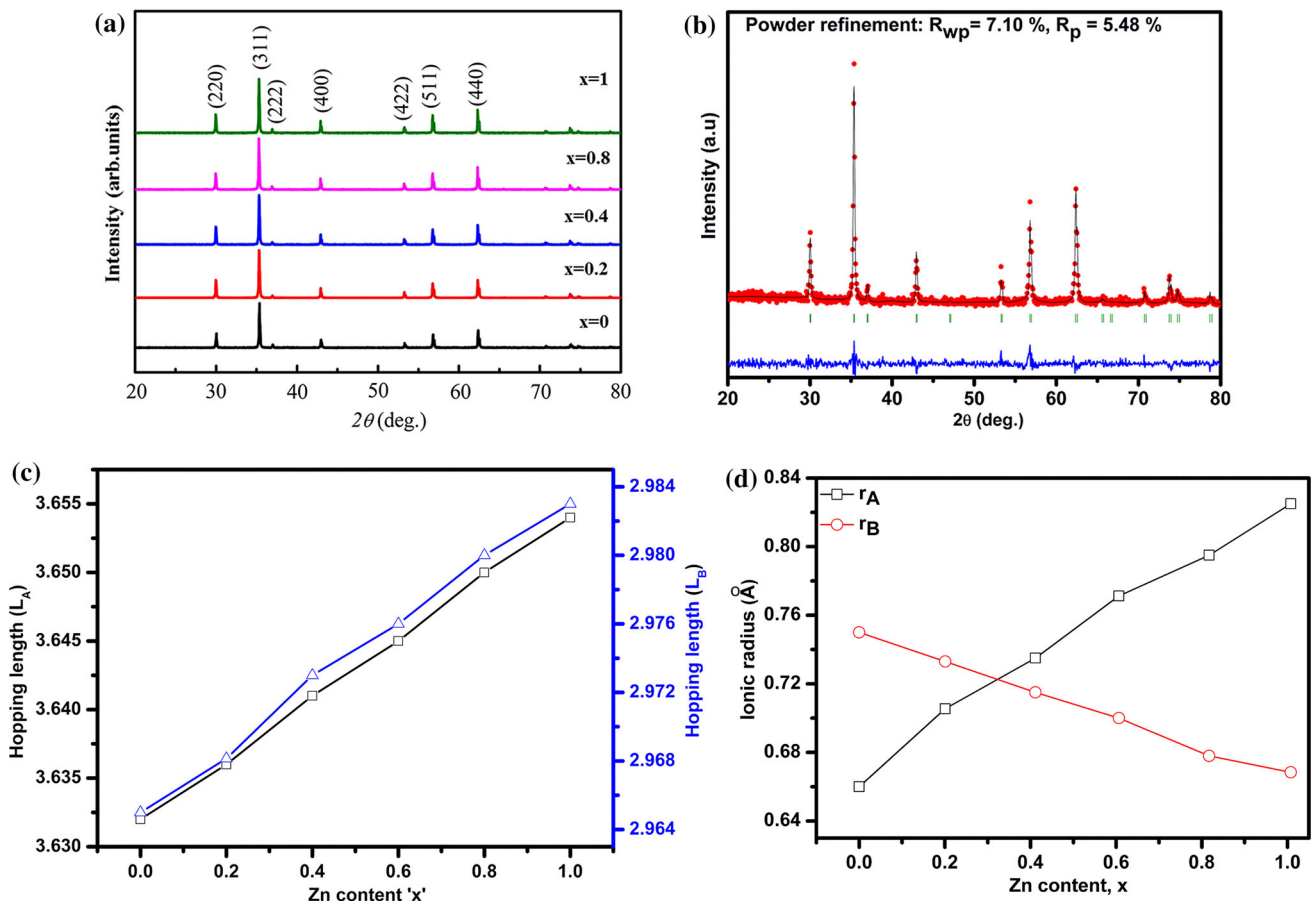


**Fig. 2** **a** XRD pattern of the ferrite system  $\text{Co}_{1-x}\text{Zn}_x\text{Fe}_2\text{O}_4$  sintered at  $900\text{ }^\circ\text{C}/15\text{ min}$ . **b** The Rietveld refinement of X-ray powder diffraction pattern for  $\text{Co}_{0.4}\text{Zn}_{0.6}\text{Fe}_2\text{O}_4$ . **c** Variation of hopping length ( $L_A$  and  $L_B$ ) with composition  $x$  for the system  $\text{Co}_{1-x}\text{Zn}_x\text{Fe}_2\text{O}_4$ . **d** Variation of ionic radius of the A-site ( $r_A$ ) and of the B-site ( $r_B$ ) of  $\text{Co}_{1-x}\text{Zn}_x\text{Fe}_2\text{O}_4$

**Table 1** Lattice constant (a), crystallite size, bulk density ( $d_{\text{bulk}}$ ), X-ray density ( $d_{\text{x-ray}}$ ), porosity (P), For  $\text{Co}_{1-x}\text{Zn}_x\text{Fe}_2\text{O}_4$

Composition 'x'	0	0.2	0.4	0.6	0.8	1.0
a (Å)	8.388	8.39	8.41	8.42	8.43	8.44
Grain size (nm)						
XRD	54	52	49	46	42	53
SEM	58	49	48	45	40	57
Bulk density ( $\text{g}/\text{cm}^3$ )	5.126	5.132	5.142	5.189	5.199	5.212
X-ray density ( $\text{g}/\text{cm}^3$ )	5.286	5.289	5.298	5.312	5.319	5.329
Porosity (%)	3	3	3	2	2	2

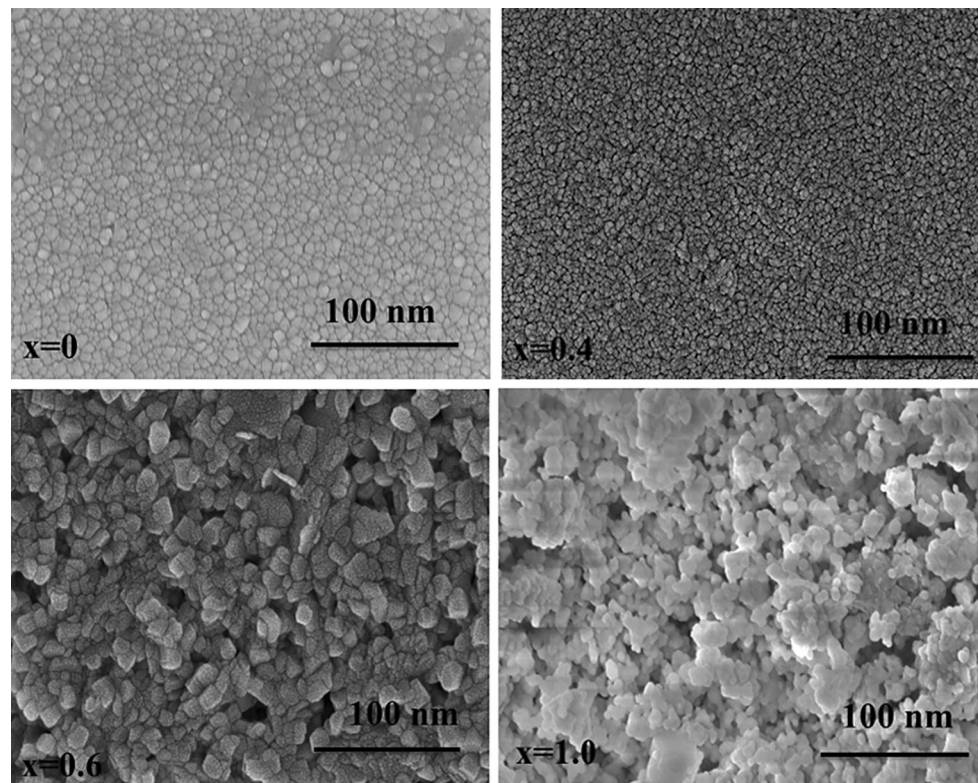
and  $L_B$  is also shown in Fig. 2c. Both  $L_A$  and  $L_B$  increases with Zn composition  $x$ . This may be attributed to the increase in lattice constant of the samples. Using the cation distribution data the mean ionic radius of tetrahedral (A) site ( $r_A$ ) and octahedral [B] site ( $r_B$ ) was calculated. It is observed from Fig. 2d that  $r_A$  increases and  $r_B$  decreases with zinc substitution. The increase in  $r_A$  is due to the replacement of  $\text{Fe}^{3+}$  ions at the tetrahedral A-site by the larger radius  $\text{Zn}^{2+}$  ions. The decrease in  $r_B$  may be due to the increasingly migration of the larger  $\text{Co}^{2+}$  ions to the octahedral B-site instead of  $\text{Fe}^{3+}$  ions.

Figure 3 shows the scanning electron microscope (SEM) images for typical samples ( $x = 0, 0.4, 0.6$  and  $1.0$ ). The average crystallite size was determined through SEM and XRD. Their values are presented in Table 1. It is observed that the crystallite size obtained from XRD data and SEM images is in good agreement with each other. The average particle size of all the samples is in between 30 and 57 nm.

Figure 4a, b show the frequency dependence of real and imaginary parts of permittivity ( $\epsilon'$  and  $\epsilon''$ ). The value of  $\epsilon'$  for  $\text{CoFe}_2\text{O}_4$  was found to be 35 and almost remained constant in the frequency 100 kHz–500 MHz. With further



**Fig. 3** FE-SEM images of  $x = 0, 0.4, 0.6$  and  $1$  of  $\text{Co}_{1-x}\text{Zn}_x\text{Fe}_2\text{O}_4$



increase of frequency the value of  $\epsilon'$  increases and shows a resonance and anti-resonance type of behavior around 1 GHz, making possible the applicability of these materials for high frequency domain. A similar behavior has been observed for all other samples under study. The dielectric constant of any material, in general, is due to dipolar, electronic, ionic and interfacial polarizations. At low frequencies dipolar and interfacial polarizations are known to play the most important role [27]. Variations in dielectric constant of ferrites have mainly been attributed to the variations in the concentration of  $\text{Fe}^{2+}$  ions [28–30]. The greater the concentration of these ions, the higher the dielectric constant expected. This is attributable to the comparatively greater polarizability of the  $\text{Fe}^{2+}$  ions, which have a greater number of electrons than the  $\text{Fe}^{3+}$  ions. In general, the polarizability of atoms with a larger number of electrons in their outer shells is more than that of atoms having relatively fewer electrons [31]. Besides,  $\text{Fe}^{3+}$  ions have a stable d-shell configuration with spherical symmetry of the charge cloud, on account of their 5d electrons distributed according to Hund's rule. In case of  $\text{Fe}^{2+}$  ions, this symmetry is disturbed on addition of an extra electron. Thus, ions would lend themselves to polarization more easily on application of an electric field than the  $\text{Fe}^{3+}$  ions where the distortion of the spherical charge cloud is relatively more difficult. The presence of  $\text{Fe}^{2+}$  ions would also result in charge transfer of the type

$\text{Fe}^{2+} \leftrightarrow \text{Fe}^{3+}$ , causing a local displacement of electrons in the direction of the electric field leading to polarization.

The decrease of dielectric constant with frequency can be explained on the basis of electron hopping conduction. In Co–Zn ferrite, the B sites are occupied by Co and Fe ions. The multiple valence ions can facilitate electron hopping on the B sites [32]. In ferrites it is well known that the samples consist of well-conducting grains separated by poorly conducting grain boundaries [30]. The electrons reach the grain boundary through hopping and if the resistance of the grain boundary is high enough, electrons pile up at the grain boundaries and produce polarization. As the field frequency increases, the dipoles will barely have started to move before the field reverses, and try to move the other way. At this stage the field is producing virtually no polarization of the dielectric. This process is generally called relaxation and the frequency beyond which the polarization no longer follows the field. Relaxation arises from the inertia of the system of charges and a restoring forces acting on the charges which oppose the force due to the applied electric field. Thus these systems combine inertia and restoring force a resonance is possible rather than relaxation. Resonance causes an increase in the displacements of the charges so that the alternating polarization, and therefore the permittivity at first rise in value. As the applied field frequency rises above the resonant frequency it passes through an antiphase condition, where

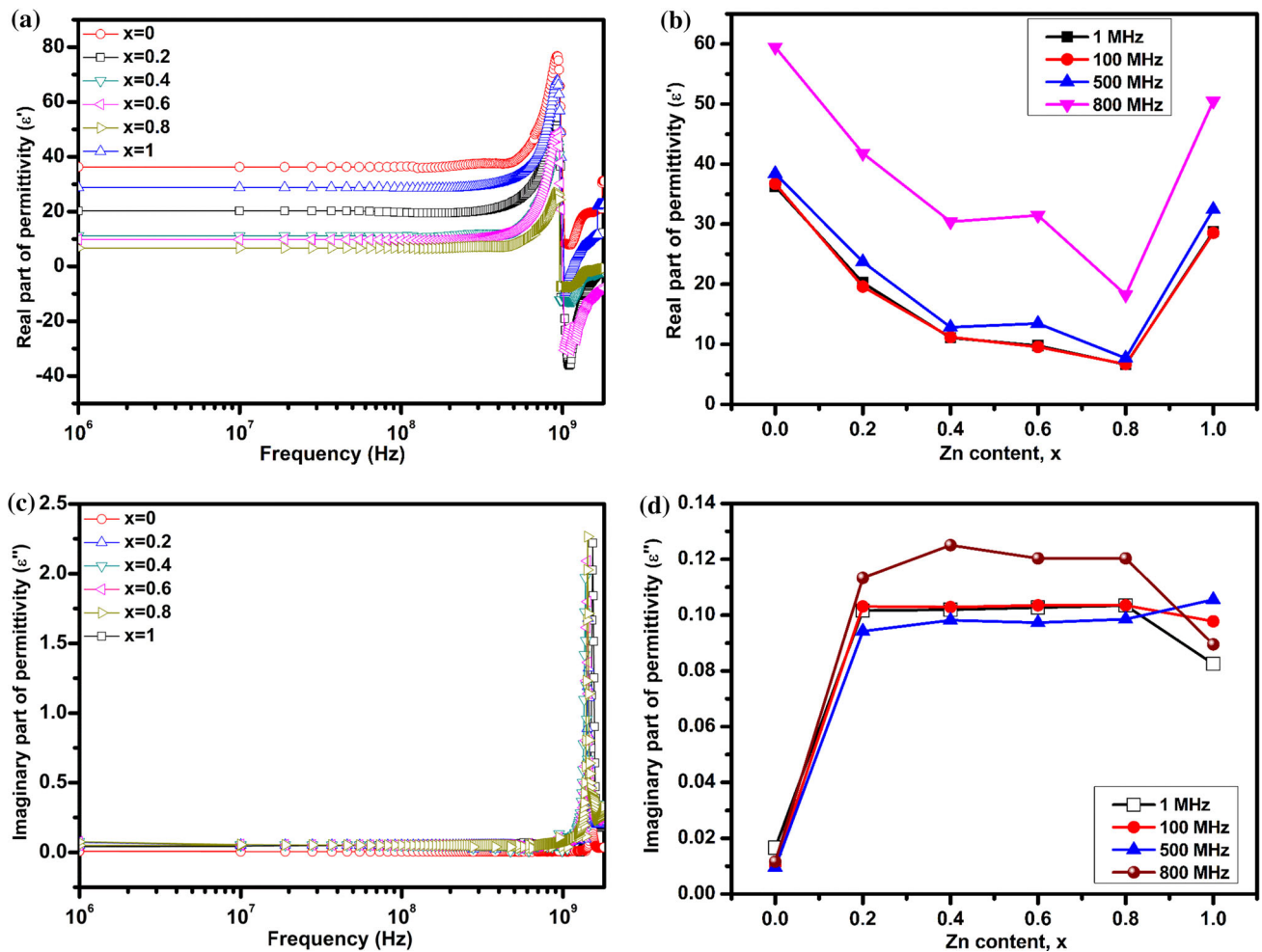


**Fig. 4** **a** Frequency variation of real part of permittivity of  $\text{Co}_{1-x}\text{Zn}_x\text{Fe}_2\text{O}_4$  ( $0 \leq x \leq 1$ ). **b** Compositional dependence of the real part of permittivity at selected frequencies for  $\text{Co}_{1-x}\text{Zn}_x\text{Fe}_2\text{O}_4$  ( $0 \leq x \leq 1$ ). **c** Frequency variation of imaginary part of permittivity

of  $\text{Co}_{1-x}\text{Zn}_x\text{Fe}_2\text{O}_4$  ( $0 \leq x \leq 1$ ). **d** Compositional dependence of the imaginary part of permittivity at selected frequencies for  $\text{Co}_{1-x}\text{Zn}_x\text{Fe}_2\text{O}_4$  ( $0 \leq x \leq 1$ )

it opposes the vibrations of the charges, and the polarization falls to a very low value. Finally, as the frequency is raised still further, complete relaxation occurs and the polarization resumes a steady value in which the particular mechanism is no longer operative. This process gives the characteristic resonance shape to the permittivity curves for ionic and electronic polarization mechanisms [33]. The dielectric constant with zinc concentration is decreasing for 1, 100, 500 MHz, but as the frequency increases to 800 MHz it again increased (Fig. 4b) following the resonance behavior of ferrites.

The frequency dependence of  $\epsilon''$  for  $\text{CoFe}_2\text{O}_4$  is 0.1 and almost remained constant with increase of frequency from 100 kHz to 1 GHz (Fig. 4c). As the zinc concentration increases  $\epsilon''$  decreased and it is highest at 100 MHz (Fig. 4d). A similar behavior has been observed for other samples. In general, dielectric loss in the case of

polycrystalline ferrites the dielectric loss is due to the lag in polarization vis-a-vis the alternating electric field. This lag increases due to the presence of impurities and imperfections in the ferrite structure, thereby increasing the dielectric loss. A major contribution to dielectric losses in ferrites comes from electron hopping between the  $\text{Fe}^{2+}$  and  $\text{Fe}^{3+}$  ions [34]. Dielectric loss for the presently investigated ferrites is found to be low and remained constant in the wide frequency range of 100 kHz–1 GHz. The lower values of dielectric loss obtained in the present work can be attributed to the curtailing of the  $\text{Fe}^{2+}$  ions on account of the synthesis process, resulting in better compositional stoichiometry and crystal structure.

Figure 5a, b shows the variation of magnetic permeability components with frequency for  $\text{CoZnFe}_2\text{O}_4$  series. The real part of permeability ( $\mu'$ ) of ferrite is influenced by wall displacement of magnetization domains at low frequencies,

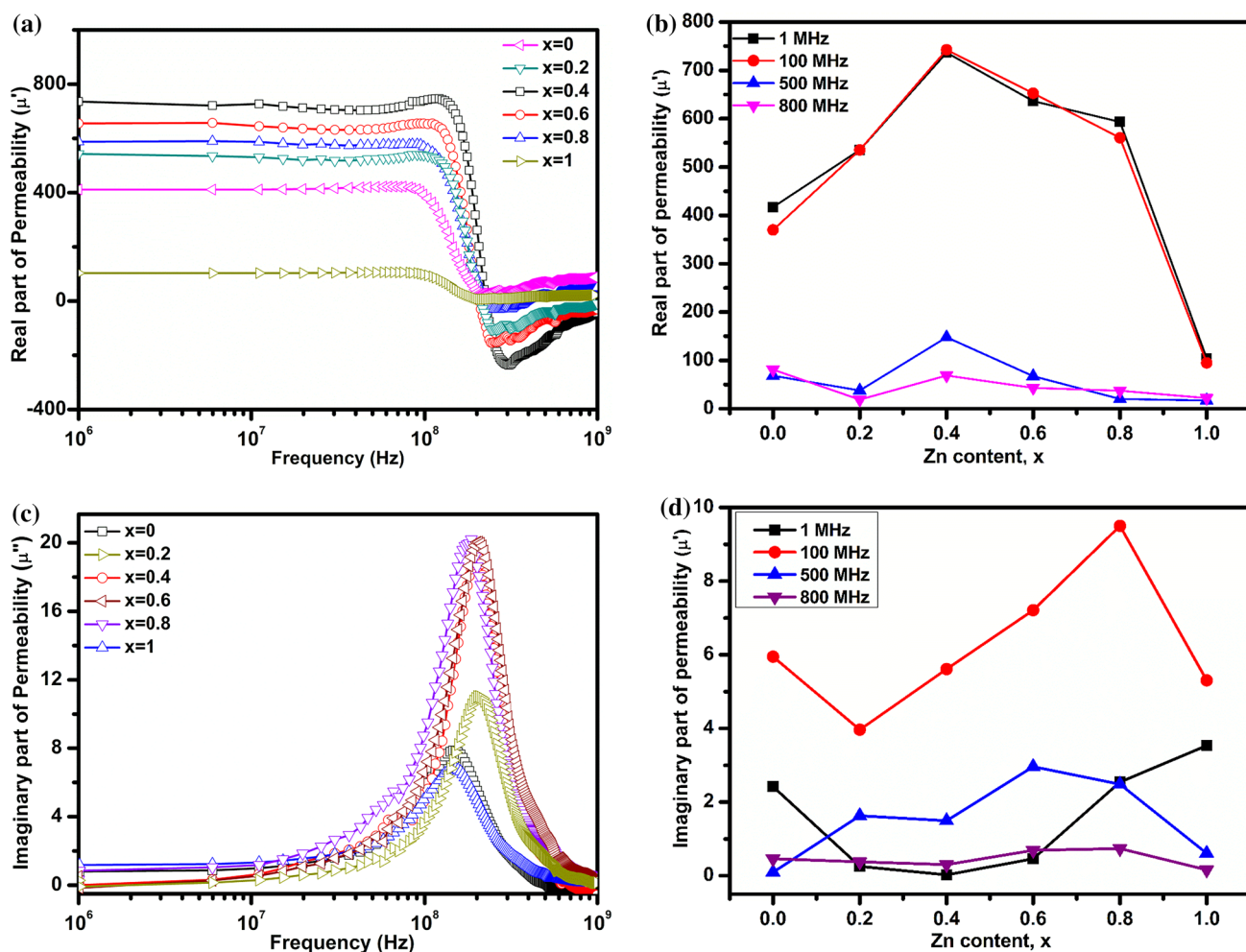


**Fig. 5** **a** Frequency variation of real part of permeability of  $\text{Co}_{1-x}\text{Zn}_x\text{Fe}_2\text{O}_4$  ( $0 \leq x \leq 1$ ). **b** Compositional dependence of the real part of permeability at selected frequencies for  $\text{Co}_{1-x}\text{Zn}_x\text{Fe}_2\text{O}_4$  ( $0 \leq x \leq 1$ ). **c** Frequency variation of imaginary part of permeability

of  $\text{Co}_{1-x}\text{Zn}_x\text{Fe}_2\text{O}_4$  ( $0 \leq x \leq 1$ ). **d** Compositional dependence of the imaginary part of permeability at selected frequencies for  $\text{Co}_{1-x}\text{Zn}_x\text{Fe}_2\text{O}_4$  ( $0 \leq x \leq 1$ )

while magnetic spin rotation at high frequencies. The highest values of real part of permeability  $\mu'$  at room temperature belong to  $x = 0.4$  and  $x = 0.6$  characterized by highest values of the average grains size and good densification. It is known that high zinc content increases the value of magnetic permeability due to the densification of samples and the increase of magnetic spin rotation contribution [35]. From Fig. 5b, it could be observed that the lower values of  $\mu''$  all the samples. The conduction mechanism in Co ferrite was explained through the existence of simultaneous conduction of n-type ( $\text{Fe}^{3+}/\text{Fe}^{2+}$ ) and p-type ( $\text{Co}^{2+}/\text{Co}^{3+}$ ) which occurs mainly between adjacent B sites, because the distances between metallic cations are sufficiently reduced to facilitate electronic transitions [36]. The real part of permeability spectrum for  $\text{CoFe}_2\text{O}_4$  shows that the value of  $\mu'$  is about 413 at 1 MHz and remains constant with an increase of frequency up to 100 MHz. With further increase

of frequency the value of  $\mu'$  is found to increase and shows a relaxation peak at around 108 MHz.

As the zinc content increases, it was found that the  $\mu'$  decreases as the frequency increases. It is exhibiting higher values than 500–800 MHz shown in Fig. 5b.

The frequency dependence of imaginary part of magnetic permeability ( $\mu''$ ) shows that the value of  $\mu''$  for all the ferrites are gradually increased with frequency and exhibits a broad maxima around 108 MHz. In contrast where the real part of permeability rapidly decreases. This phenomena is well known as natural resonance [37, 38]. As 'x' was increased, the natural resonance frequency, where the imaginary permeability had a maximum value, shifts towards higher frequency side. Zinc concentration dependent  $\mu''$  is plotted in Fig. 5d, it is found that at 100 MHz the  $\mu''$  is showing high loss than the other frequencies, i.e. after the resonance frequency (108 MHz).

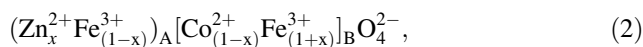


Figure 6 shows the variation of magnetization with the applied field. All prepared samples at room temperature exhibit ferrimagnetic coupling. As zinc is introduced in the system, it pushes Fe<sup>3+</sup> ions from tetrahedral A sites to octahedral B sites [39]. This causes the increase in magnetization of Co<sub>1-x</sub>Zn<sub>x</sub>Fe<sub>2</sub>O<sub>4</sub>. That is, while the magnetic moment of the A site decreases due to increase of non-magnetic Zn ions in the A site, the magnetic moment of the B site increases due to increase of Fe<sup>3+</sup> ions in B site. Therefore, in present study, when the Zn concentration increases from 0 to 0.2, total magnetization (M<sub>oct</sub> - M<sub>tet</sub>) increases because of the increase of inter-sublattice A–B super-exchange interaction between the magnetic ions of the sublattices A and B. This increase in saturation magnetization with Zn concentration from x = 0.0 to x = 0.2 is in good agreement with Neel’s collinear two-sublattice model [40], further increase in the Zn concentration from x = 0.2 to x = 1.0, the saturation magnetization gradually decreases from 79.04 to 26.04 emu/g. The results obtained are in well accordance with the earlier reported values [41, 42]. The coercivity also decreases with Zn concentration which is attributed to the non-magnetic character of Zn ion. Since more Zn ions replace with Co ions by increasing ‘x’, the saturation magnetization and coercivity decreases.

According to Neel’s two sublattice model of ferromagnetism, the magnetic moments of ions on the tetrahedral (A) and octahedral (B) sites are aligned antiparallel to each other and spins have collinear structure. Therefore, the theoretic magnetic moment per formula unit in μ<sub>B</sub>, n<sub>B</sub><sup>t</sup>, is described as

$$n_B^t(x) = M_B(x) - M_A(x), \tag{1}$$

where M<sub>B</sub>(x) and M<sub>A</sub>(x) are the B and A sublattice magnetic moments in μ<sub>B</sub>, respectively. The cation distribution of the Co<sub>1-x</sub>Zn<sub>x</sub>Fe<sub>2</sub>O<sub>4</sub> can be written as



As a function of Zn concentration, the theoretic magnetic moment values, n<sub>B</sub><sup>t</sup>, of the Co<sub>1-x</sub>Zn<sub>x</sub>Fe<sub>2</sub>O<sub>4</sub> were calculated using the cation distribution given in Eq. 2. The ionic magnetic moments of Fe<sup>3+</sup>, Co<sup>2+</sup>, and Zn<sup>2+</sup> as 4.85, 2.78 and 0 μ<sub>B</sub>, respectively. The experimental values of the magnetic moments (n<sub>B</sub><sup>e</sup>), per unit formula in Bohr magneton (μ<sub>B</sub>) were calculated according to the relation [37]

$$n_B^e = \frac{M_w \cdot M_s}{5585}, \tag{3}$$

where M<sub>w</sub> is the molecular weight, M<sub>s</sub> is the saturation magnetization and 5585 is the magnetic factor. The variation of the theoretic magnetic moment and experimental magnetic moment (n<sub>B</sub><sup>t</sup> and n<sub>B</sub><sup>e</sup> respectively) with respect to Zn composition is represented in Table 2. The theoretic magnetic moment increases linearly as a function of Zn concentration, and the experimental magnetic moment, increases with Zn concentration of up to x = 0.2 and then gradually decreases with further increase in Zn concentration. This increase in n<sub>B</sub><sup>e</sup> with Zn concentration of up to x = 0.2 can be attributed to the Neel’s collinear two-sublattice model. However, this model is unable to explain the decrease of n<sub>B</sub><sup>e</sup> (and hence M<sub>s</sub>) with Zn concentration for x > 0.2. The decrease in n<sub>B</sub><sup>t</sup> (and hence M<sub>s</sub>) for x > 0.2, which results from the existence of noncollinear spin arrangement in the system, could be explained on the basis of the three-sublattice model suggested by Yafet and Kittel [43]. When higher Co<sup>2+</sup> ions are substituted by Zn<sup>2+</sup> ions in the Co<sub>1-x</sub>Zn<sub>x</sub>Fe<sub>2</sub>O<sub>4</sub>, the magnetic ions of tetrahedral A site are so much decreased that the dominant inter-sublattice A–B super-exchange interaction becomes weaker and hence the intra-sublattice B–B super-exchange interaction strengthens, which in turn results in occurrence of random spin canting on the B site with respect to the direction of spins of the A site. Therefore, it can be reasonably concluded that the canted (non-collinear) spins lead to a decrease in the values of the experimental magnetic moment (and thus the magnetization) with Zn concentration for x > 0.2.

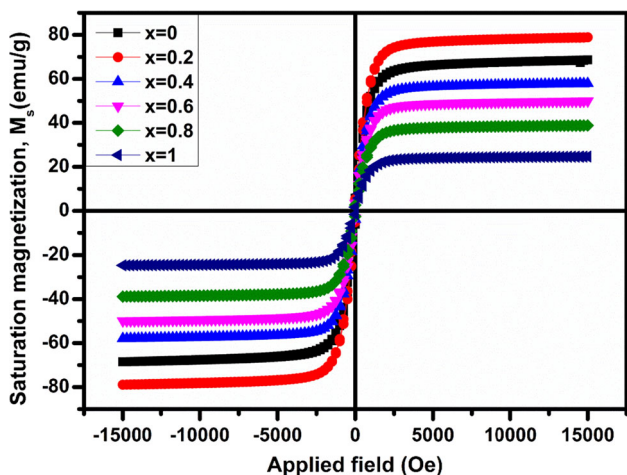


Fig. 6 The magnetic hysteresis loops of Co<sub>1-x</sub>Zn<sub>x</sub>Fe<sub>2</sub>O<sub>4</sub> (0 ≤ x ≤ 1) at room temperature

Table 2 Data of saturation magnetization (M<sub>s</sub>) for RT, magnetic moment (experimental and theoretic), Y–K angle (α<sub>YK</sub>) for Co<sub>1-x</sub>Zn<sub>x</sub>Fe<sub>2</sub>O<sub>4</sub> system

‘x’	M <sub>s</sub> (emu/g) RT	α <sub>YK</sub> (°)	n <sub>B</sub> <sup>e</sup> (μ <sub>B</sub> )	n <sub>B</sub> <sup>t</sup> (μ <sub>B</sub> )
0	68.71	3.8	3.12	2.98
0.2	79.04	29.56	3.25	4.2
0.4	57.7	51.63	2.56	5.9
0.6	50.82	63.86	2.12	7.2
0.8	39.12	74.31	0.98	8.8
1	26.04	84.6	0.2	10.05



The significant difference between the experimental and theoretic magnetic moment values suggests that the magnetic order in the present ferrite system is not governed by the Neel-type magnetic order, but by the Y–K type magnetic order [44, 45]. According to the Y–K model, the B lattice can be divided into two sublattices  $B_1$  and  $B_2$ , each having magnetic moments equal in magnitude and each oppositely canted at the same angle,  $\alpha_{YK}$ , relative to the net magnetization at 0 K. In this way, the two sublattices  $B_1$  and  $B_2$  have the triangular spin arrangement which becomes more significant with the changing concentration. The existence of canted spin and the behaviour of the magnetic moment with increasing Zn concentration can be observed by determining the Y–K angle ( $\alpha_{YK}$ ). The values of the Yafet and Kittle (Y–K) angle have been calculated using the formula

$$n_B^e = M_B \cos \alpha_{Y-K} - M_A, \quad (4)$$

where  $n_B^e$  is the experimental magnetic moment expressed in the units of Bohr magneton and  $M_A$  and  $M_B$  are the Bohr magneton on the A site and B sites, respectively. The variation of the calculated Y–K angles for different concentrations of the system is shown in Fig. 7. The values of the Y–K angles for each sample are listed in Table 2. The Y–K angle is zero for  $x = 0.0$ , indicating that the magnetization can be explained on the basis of the Neel's two-sublattice theory for only the sample with  $x = 0.0$  in the present study. That is,  $\text{CoFe}_2\text{O}_4$  show a Neel-type of magnetic ordering. It is clear from Fig. 7 that the calculated value of the Y–K angles gradually increases with the increase of Zn concentration and finally extrapolates  $84.37^\circ$  for the  $\text{ZnFe}_2\text{O}_4$  ( $x = 1.0$ ).

The non-zero Y–K angles suggest that for all the samples (for  $x > 0$ ) the magnetization behaviour cannot be explained on the Neel two-sublattice model due to the

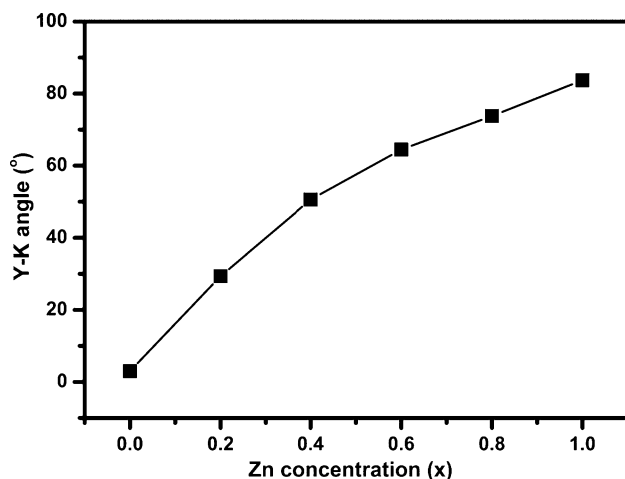


**Fig. 7** The variation of Y–K angle with Zn concentration of  $\text{Co}_{1-x}\text{Zn}_x\text{Fe}_2\text{O}_4$  ( $0 \leq x \leq 1$ )

presence of non-collinear spin structure on B sites, which strengthens the B–B interaction and thus decreases the A–B interaction. The increase in spin canting angles (Y–K angles) for the samples with  $x > 0$  with the increase in Zn content suggests the increased favour for triangular spin arrangements on B sites resulting in the decrease of A–B exchange interaction and the existence of canted spin arrangements in all the samples (for  $x > 0.0$ ) under consideration in this study. Therefore, it also leads to a reduction in saturation magnetization after Zn concentration with  $x > 0.2$  and also increase of randomness and frustration, showing significant departure from the Neel-type collinear magnetic order [46]. It is concluded from the evaluation of Y–K angles for  $\text{Co}_{1-x}\text{Zn}_x\text{Fe}_2\text{O}_4$  ( $0 \leq x \leq 1$ ) that the  $\text{Co}_{1-x}\text{Zn}_x\text{Fe}_2\text{O}_4$   $x > 0.0$  have a Y–K-type magnetic order, while the  $\text{CoFe}_2\text{O}_4$  NPs ( $x = 0.0$ ) have a Neel-type magnetic order. In other words, in this study, all the Zn-doped cobalt ferrite nanoparticles show a Y–K type of magnetic ordering except the pure  $\text{CoFe}_2\text{O}_4$ .

The variation of remnant magnetization ( $M_r$ ) with Zn concentration at room temperature is depicted in Fig. 8. The inset in Fig. 8 shows the change in the reduced remnant magnetization ( $M_r/M_s$ ) with the Zn concentration. As shown the  $M_r$  of this ( $0.6 \leq x \leq 1.0$ )  $M_r/M_s$  is zero, which proves that these samples are superparamagnetic at room temperature. As shown in the inset in Fig. 8, the  $M_r/M_s$  gradually decreases with increasing Zn concentration and all  $M_r/M_s$  values are lower than the theoretic value of 0.5. This can be explained with decreasing magnetic anisotropy depending on the increasing Zn concentration [47]. According to the Stoner–Wohlfarth model [48],  $M_r/M_s$  for an assembly of non-interacting 3D random particles is given by  $M_r/M_s = 0.5$  for uniaxial anisotropy and  $M_r/M_s = 0.832$  for cubic anisotropy. These reduced remnant

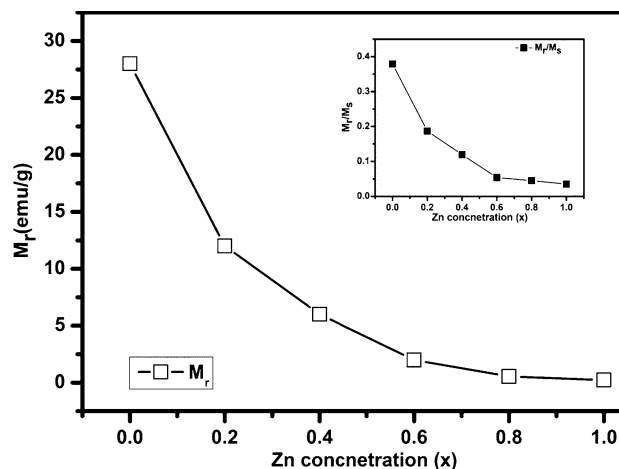


**Fig. 8** The remnant magnetization versus Zn concentration taken at room temperature for the  $\text{Co}_{1-x}\text{Zn}_x\text{Fe}_2\text{O}_4$  (inset presents the change in reduced remnant magnetization ( $M_r/M_s$ ) with Zn content)

magnetization values observed in the inset in Fig. 8 are more in agreement with uniaxial anisotropy rather than the expected cubic anisotropy according to the Stoner–Wohlfarth model. Therefore, it can be concluded that all the samples used in this study have uniaxial anisotropy because their reduced remnant magnetization values are lower than 0.5. Cobalt-substituted ferrite nanoparticles with uniaxial anisotropy have been reported previously [49, 50]. The uniaxial anisotropy in magnetic nanoparticles can arise from surface effects [51]. The lower  $M_r/M_s$  values than 0.3 found for the samples with  $x = 0.2$  and 0.4 in this study suggest that the interactions between the nanoparticles are not negligible [52].

Figure 9 shows the variation of the coercive field ( $H_c$ ) and effective magnetic anisotropy constant ( $K_{\text{eff}}$ ) with respect to Zn concentration at room temperature. It can be easily seen from Fig. 9 that  $H_c$  and  $K_{\text{eff}}$  decrease with increasing Zn concentration. According to the Stoner–Wohlfarth model,  $H_c$  for an assembly of non-interacting 3D random particles is given by  $H_c = 0.985 K_{\text{eff}}/M_s$  for uniaxial anisotropy and  $H_c = 0.64 K_{\text{eff}}/M_s$  for cubic anisotropy. It was found from the  $M_r/M_s$  results that all the samples in this study have uniaxial anisotropy. Therefore, to calculate the  $K_{\text{eff}}$ , the relation  $H_c = 0.64 K_{\text{eff}}/M_s$  was used. As shown from Figs. 7, 8 and 9, the  $H_c$  is almost negligible at room temperature for  $0.6 \leq x \leq 1.0$ , indicating the existence of superparamagnetic behaviour for only these samples. The coercive field is associated to the strength of the magnetic field that is required to overcome the anisotropy barrier. According to the Stoner–Wohlfarth theory, magnetic anisotropy energy ( $E_A$ ) for non-interacting single-domain particles is given by

$$E_A = KV \sin^2 \theta, \quad (5)$$

where  $K$ ,  $V$ , and  $\theta$  are magnetic anisotropy energy constant, volume of the particles, and the angle between

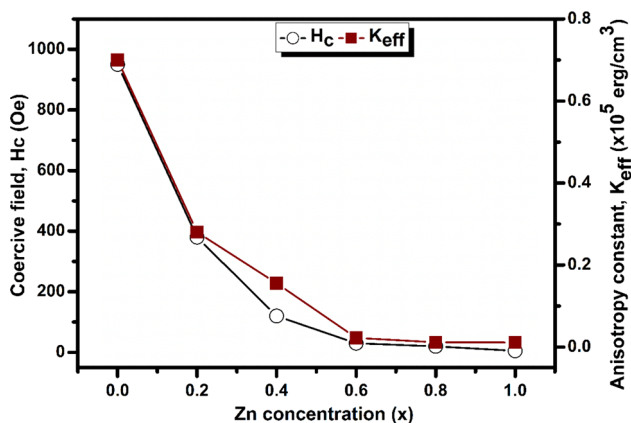


**Fig. 9** Composition dependence of coercive field ( $H_c$ ) and effective magnetic anisotropy constant ( $K_{\text{eff}}$ ) of  $\text{Co}_{1-x}\text{Zn}_x\text{Fe}_2\text{O}_4$  at room temperature

magnetization direction and the easy axis of a nanoparticles, respectively. With reducing of magnetic anisotropy, the magnetic anisotropy energy barrier ( $E_A$ ) decreases, which causes lower external magnetic field for spin reversal. The strong magnetocrystalline anisotropy of cobalt ferrite is mainly due to the presence of  $\text{Co}^{2+}$  ions in the octahedral (B) sites of the spinel structure [53]. When the Zn concentration increases in cobalt ferrite, the concentration of the  $\text{Co}^{2+}$  ions in the octahedral (B) sites decreases, which leads to decreasing the effective magnetic anisotropy. Therefore, in this study, the effective magnetic anisotropy,  $K_{\text{eff}}$  and accordingly  $H_c$  of the samples decrease with increasing Zn concentration. The decreasing of  $K_{\text{eff}}$  and  $H_c$  with increasing Zn concentration is generally the expected behavior in the metal-substituted ferrite particles [54, 55].

## 4 Conclusions

$\text{Co}_{1-x}\text{Zn}_x\text{Fe}_2\text{O}_4$  XRD patterns are sharp and intense and show the reflection which belongs to cubic spinel structure. The FTIR measurements between 400 and 4000  $\text{cm}^{-1}$  confirmed the intrinsic cation vibrations in the spinel. The lattice constant increases with zinc substitution. X-ray and bulk density increases with zinc substitution. Room temperature ferromagnetic ordering is observed in samples. The dielectric properties were influenced by Zn substitution and were explained by the electron hopping mechanism between  $\text{Fe}^{2+}$  and  $\text{Fe}^{3+}$  ions. The magnetic properties are explained in terms of cation distribution and grain size effect. Thus high permeability, moderate  $M_s$  and  $H_c$  exhibited by the Zn doped  $\text{CoFe}_2\text{O}_4$  nanocrystals are favorable for their potential use in high density recording media applications as ferrite *head*.

**Acknowledgments** Dr. K. Praveena acknowledges the Ministry of Science and Technology of Republic of China under Grant No. MOST 104-2811-M-003-009 and National Science Council, Taiwan under Grant No. NSC 102-2112-M-003-002-MY3 for financial support.

## References

1. K. Praveena, S. Srinath, J. Nanosci. Nanotechnol. **14**, 4371 (2014)
2. K. Praveena, B. Radhika, S. Srintah, AIP Conf. Proc. **1447**, 289 (2012)
3. X.J. Zhang, W. Jiang, D. Song, H.J. Sun, Z.D. Sun, F.S. Li, J. Alloys Compd. **475**, 34 (2009)
4. K. Praveena, S.R. Murthy, Magneto acoustical emission in nanocrystalline Mn–Zn ferrites. Mater. Res. Bull. **48**, 4826 (2013)
5. M. Ben Ali, K. El Maalam, H. El Moussaoui, O. Mounkachi, M. Hamedoun, R. Masrour, E.K. Hlil, A. Benyoussef, J. Magn. Mater. **398**, 20 (2016)

6. S. Bastien, N. Braidy, J. Appl. Phys. **114**, 214304 (2013)
7. K. Sadhana, R. Sandhya, S.R. Murthy, K. Praveena, Mater. Sci. Semicond. Process. **40**, 578 (2015)
8. P. Kuruva, S. Matteppanavar, S. Srinath, T. Thomas, IEEE Trans. Magn. **50**, 5200108 (2014)
9. Q. Chen, Z. John, Zhang. Appl. Phys. Lett. **73**, 3156 (1998)
10. Z.X. Tang, C.M. Sorensen, K.J. Klabunde, Phys. Rev. Lett. **67**, 3602 (1991)
11. K.J. Davies, S. Wells, R.V. Upadhyay, S.W. Charles, K. O'Grady, M. El Hilo, T. Meaz, S. Mørup, J. Magn. Magn. Mater. **149**, 14 (1995)
12. K. Praveena, K.B.R. Varma, J. Mater. Sci.: Mater. Electron. **25**, 111 (2014)
13. M.A. Lopez-Quintela, J. Rivas, J. Colloid Interface Sci. **158**, 446 (1993)
14. G.A. Pettit, D.W. Forester, Phys. Rev. B **4**, 3912 (1971)
15. V.J. Angadi, B. Rudraswamy, K. Sadhana, S.R. Murthy, K. Praveena, J. Alloys Compd. **656**, 5 (2016)
16. J. Ding, P.G. Mc Cormick, R. Street, J. Magn. Magn. Mater. **171**, 309 (1997)
17. S. Komarneni, R. Roy, Q.-H. Li, Mater. Res. Bull. **27**, 1393 (1992)
18. C. Huo, H. Yu, Q. Zhang, Y. Li, H. Wang, J. Alloys Compd. **491**, 431 (2010)
19. S.B. Waje, M. Hashim, W.D.W. Yusoff, Z. Abbas, J. Magn. Magn. Mater. **322**, 686 (2010)
20. D.M.R. Mingos, D.R. Baghurst, Chem. Soc. Rev. **20**, 1 (1991)
21. V.G. Patil, S.E. Shirsath, S.D. Morec, S.J. Shukla, K.M. Jadhav, J. Alloys Compd. **488**, 199 (2009)
22. M. Sertkol, Y. Koseoglu, A. Baykal, H. Kavas, A. Bozkurt, M.S. Toprak, J. Alloys Compd. **479**, 49 (2009)
23. B.D. Cullity, *Elements of X-ray Diffraction*, vol. 99 (Addison-Wesley Publ. Comp. Inc., Reading, 1956)
24. R.A. Young, *The Rietveld Method* (Oxford University Press, Oxford, 1993)
25. A.K.M. Akther Hossain, S.T. Mahmud, M. Seki, T. Kawai, H. Tabata, J. Magn. Magn. Mater. **312**, 210 (2007)
26. S. Kumar, V. Singh, S. Aggarwal, U.K. Mandal, R.K. Kotnala, J. Phys. Chem. C **114**, 6272 (2010)
27. A.K. Singh, T.C. Goel, R.G. Mendiratta, O.P. Thakur, C. Prakash, J. Appl. Phys. **91**, 6626 (2002)
28. N. Rezlescu, E. Rezlescu, Phys. Stat. Sol. (a) **23**, 575 (1974)
29. J.T.S. Irvine, A. Huanosta, R. Velenzuela, A.R. West, J. Am. Ceram. Soc. **73**, 729 (1990)
30. C.G. Koops, Phys. Rev. **83**, 121 (1951)
31. L.L. Hench, J.K. West, *Principles of Electronic Ceramics* (Wiley, New York, 1990), p. 346
32. N. Rezlescu, E. Rezlescu, P.D. Popa, M.L. Craus, L. Rezlescu, J. Magn. Magn. Mater. **182**, 199 (1998)
33. J.C. Anderson, K.D. Leaver, J.M. Alexander, R.D. Tawlings, *Materials Science*, 2nd edn. (Great Britain by Thomas Nelson and sons Ltd., Nashville, 1974)
34. L.G. Van Uitert, J. Chem. Phys. **23**, 1883 (1955)
35. M.M. Haque, M. Huq, M.A. Hakim, Phys. B **404**, 3915 (2009)
36. J.S. Ghodake, R.C. Kambale, S.V. Salvi, S.R. Sawant, S.S. Suryavanshi, J. Alloys Compd. **486**, 830 (2009)
37. J. Smit, H.P.J. Wijn, *Ferrites* (Phillips Technical Library Eindhoven, Eindhoven, 1959), p. 134
38. J.L. Snoek, Physica **4**, 207 (1948)
39. C. Upadhyay, H.C. Verma, S. Anand, J. Appl. Phys. **95**, 5746 (2004)
40. L. Neel, C. R. Acad. Sci. Paris **230**, 375 (1950)
41. G. Vaidyanathan, S. Sendhilnathan, R. Arulmurugan, J. Magn. Magn. Mater. **313**, 293 (2007)
42. M.U. Islam, M.U. Rana, T. Abbas, Mater. Chem. Phys. **57**, 190 (1998)
43. Y. Yafet, C. Kittel, Phys. Rev. **87**, 290 (1952)
44. A.K.M. Akther Hossain, M.L. Rahman, J. Magn. Magn. Mater. **323**, 1954 (2011)
45. D.S. Birajdar, D.R. Mane, S.S. More, V.B. Kawade, K.M. Jadhav, Mater. Lett. **59**(24–25), 2981 (2005)
46. M. Ajmal, A. Maqsood, J. Alloys Compd. **460**, 54 (2008)
47. J.H. Fendler, *Nanoparticles and Nanostructured Films* (Wiley, New York, 1998), p. 81
48. E.C. Stoner, E.P. Wohlfarth, Philosophical transactions of the royal society of London. Ser. A Math. Phys. Sci. **240**, 599 (1948)
49. L. Victoria, D.C. Clero-del, C. Rinaldi, J. Magn. Magn. Mater. **314**, 60 (2007)
50. S. Ammar, A. Helfen, N. Jouini, F. Fievet, I. Rosenman, F. Villain, P. Molinie, M. Danot, J. Mater. Chem. (Royal Society of Chemistry, UK) **11**, 186 (2001)
51. R.H. Kodama, J. Magn. Magn. Mater. **200**, 359 (1999)
52. G. Hadjipanayis, D.J. Sellmyer, B. Brandt, Phys. Rev. B **23**, 3349 (1981)
53. M. Tachiki, Prog. Theor. Phys. **23**, 1055 (1960)
54. S.S. Jadhav, S.E. Shirsath, S.M. Patange, K.M. Jadhav, J. Appl. Phys. **108**, 093920 (2010)
55. Y. Koseoglu, F. Alan, M. Tan, R. Yilgin, M. Ozturk, Ceram. Int. **38**, 3625 (2012)